Intermediate-field effects and the Hall resistivity in the basal plane of cadmium

C. M. Hurd, J. E. A. Alderson, and S. P. McAlister

National Research Council of Canada, Ottawa, Canada K1A OR9

(Received 8 March 1976)

The Hall resistivity $\rho_{21}(\vec{B}, T)$ ($\vec{B} \parallel$ [0001], $\vec{J} \parallel$ [10$\bar{1}$0]) has been measured in a monocrystal of Cd in the temperature range 1.5–580°K and in applied fields up to 2.0 T. At low temperatures ρ_{21} is highly sensitive to minute traces of impurity and to misalignment of the sample. To eliminate the uncertainties which arise from these sources in any comparison of ρ_{21} between different samples, we chose to make an intensive study of a single well-oriented sample. This leads to clearly defined systematic tendencies in $\rho_{21}(\vec{B}, T)$. Using path-integral calculations based upon a simple model of the second-zone "monster" that allows intersheet scattering, we are able to give a plausible qualitative description of all the observed features. We are able to show, furthermore, how this interpretation encompasses a behavior previously observed in lightly doped samples that was seemingly inconsistent with the intersheet scattering mechanism.

I. INTRODUCTION

Electrons moving parallel to the basal plane in cadmium under the influence of a magnetic flux $\vec{B}$ applied along the hexagonal axis can be divided into two classes. The first contains those electrons for which a Bragg reflection is a frequent experience during their mean free lifetime between momentum-changing collisions. The result is that their overall response to $\vec{B}$ is hole-like. In reciprocal space this class is represented by points lying on either of the hole parts of the reconstructed Fermi surface, which are the "caps" of the first Brillouin zone and the trifoliate surface formed from the "monster" of the second zone.[1] The second class contains electrons having momentum vectors such that they rarely experience a Bragg reflection during their lifetime. Their response is therefore electron-like—although not necessarily very free-electron-like—and they are represented by points lying on the electron "lens" of the third zone.

Except at the very lowest temperatures, conduction in any direction parallel to the basal plane is apparently dominated by charge carriers from the first of the above classes, for we show that the sign of the Hall effect is positive in the whole range from about 4°K up to the melting point. This domination can be understood qualitatively from the topology of the Fermi surface. The electrons represented on the lens have velocity vectors directed principally along the hexagonal axis and are therefore not major contributors to any conduction parallel to the basal plane. Furthermore, the typical effective mass associated with the hole surfaces is considerably lower than that for the electron one.[2] Consequently the holelike carriers moving parallel to the basal plane are not only more numerous but also more mobile than the electronlike ones.

Below about 4°K this domination is sharply destroyed when a field exceeding a fraction of a tesla is applied along the hexagonal axis. The sign of the Hall effect becomes suddenly very negative, while its field and temperature dependences indicate that the carrier compensation for this orientation has been effectively destroyed.[2-4] This detail in the metal's behavior has received considerable attention in recent years,[2-7] and a particular mechanism—known as *intersheet scattering*—has been proposed[7] to account for the shift from domination by holelike to domination by electronlike carriers. In addition to this singular feature, the temperature dependence of the Hall effect observed in a carefully aligned sample shows over a wider temperature range other characteristics, such as a stationary value and marked general tendencies. Our aim is to suggest a qualitative explanation of these features, and to show how it reflects upon the difficulties encountered in earlier studies[2,4] of doped samples, where the behavior seemingly did not fit with the expectations of intersheet scattering.[4]

The principal experiments to be described involve the measurement of the Hall resistivity and transverse magnetoresistance in an oriented monocrystal of pure Cd over the ranges 0.1–2.0 T and 1.5–580°K. These data are given in Sec. II. Section III describes a model used for path-integral calculations, giving the results that are discussed and compared with experiment in Sec. IV. Section V describes comparative results obtained for two oriented monocrystals of Cd containing Zn that bear upon the qualitative interpretation of Sec. IV. Our conclusions are given in Sec. VI, while the Appendix contains a brief outline of the path-integral calculations.

II. EXPERIMENTAL METHOD AND RESULTS

The sample of pure Cd was prepared by the Bridgman method exactly as described previously[8] for Cu. A monocrystalline sheet having the approximate dimensions $2 \times 8 \times 0.09$ cm^3 was prepared from starting material supplied by Alpha Inorganics (Ventron Corp.) of 99.9999% purity referred to metallic contaminants. A high-purity graphite mold was used in which the crystallographic orientation of the final crystal could be controlled with respect to that of a previously prepared seed crystal. The final sample was oriented such that the hexagonal axis was perpendicular to its plane face to within the accuracy of our back-reflection Laue techniques ($\sim 1°$). The desired sample shape was produced from the monocrystalline sheet by spark erosion using a template having the dimensions specified previously.[9] The orientation was chosen so that the primary current of 1 A lay along a $[10\bar{1}0]$ direction. The residual-resistance ratio ($R_{273\,°K}/R_{1.7\,°K}$) of the sample was 25 600.

The monocrystalline alloy samples were produced in exactly the same way except that the starting material was a previously prepared alloy of slightly higher than desired solute concentration chosen to offset the zone-refining effect inherent in the Bridgman method. Cutoffs from the top and bottom of each sample were analyzed by atomic absorption methods in our Analysis Section. The results are quoted in the caption to Fig. 9, together with the value of the corresponding residual-resistance ratio.

Measurements were made with a conventional cryostat-electromagnet combination giving a temperature range of 1.5–300 °K in fields up to 2.0 T. In the cryostat the sample could be tilted through small angles, while the electromagnet could be rotated, so that the fine adjustment of the applied fields's direction along the $[0001]$ axis could be made empirically from observations of the low-temperature magnetoresistance. The final coincidence of these vectors was made to within about 0.1°. For temperatures in the range 300–580 °K a conventional vacuum furnace was constructed to replace the cryostat. The instrumentation and techniques used to determine the galvanomagnetic voltages were identical to those described previously.[9]

Because the quantitative details of the low-temperature dependence of the Hall effect for this orientation are known to be very sensitive to errors arising from trace impurities and positioning of the $[0001]$ direction with respect to the applied field, a comparison of the Hall effect between different but otherwise seemingly identical samples
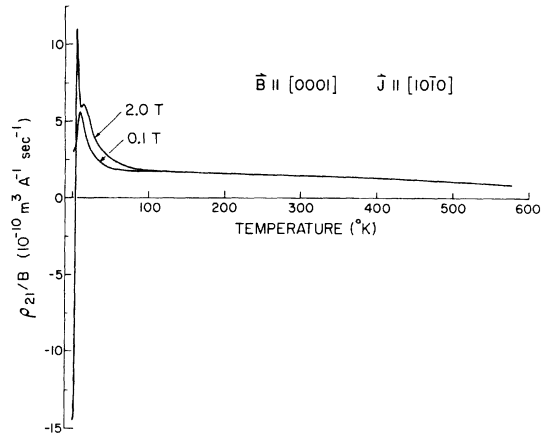

FIG. 1. Comparison of the temperature dependence of the Hall resistivity ρ_{21} (here divided by the applied flux density for easier graphical presentation) observed at the extremes of the range of applied field. A detectable field dependence exists up to about 140°K. The sample's residual-resistance ratio is 25 600. An enlarged view of the lower temperature range is shown in Fig. 2.

is confounded by erratic uncertainties[2–4] which upset the systematic tendencies. To avoid this problem, we chose specifically to study the field and temperature dependences of a single well-oriented sample. The temperature dependence of the Hall resistivity measured in this sample over the range 1.5–580 °K is shown in Fig. 1. A more complete set of data for the limited range 1.5–38 °K is shown in Fig. 2. The experimental precision of any datum in Fig. 2 is controlled primarily by the precision of the voltage measurement, which is about ± 1 nV. In the units of the abscissa of Fig. 2 this corresponds to an uncertainty of about ± 0.1 (10^{-10} m^3 A^{-1} sec^{-1}). The accuracy of a given datum in Fig. 2 is dominated by the error in the determination of the sample's thickness. This quantity (of magnitude ~ 0.09 cm) could be measured[9] to within about ± 0.0015 cm, which gives an uncertainty of about $\pm 1.6\%$ in the absolute value of the abscissa of any point in Fig. 2. Finally, Fig. 3 shows the corresponding transverse magnetoresistance $\Delta\rho/\rho_{11}(0)$, where $\Delta\rho = \rho_{11}(\vec{B}, T) - \rho_{11}(0, T)$ enters the discussion of Sec. IV.

III. MODEL OF TRIFOLIATE SURFACE

It is pointed out in Sec. I that, apart from the temperature range below about 4 °K, conduction parallel to the basal plane is dominated by carriers that have a relatively high mobility and show a holelike response to the external field (Fig. 1). The overwhelming majority of these are repre-
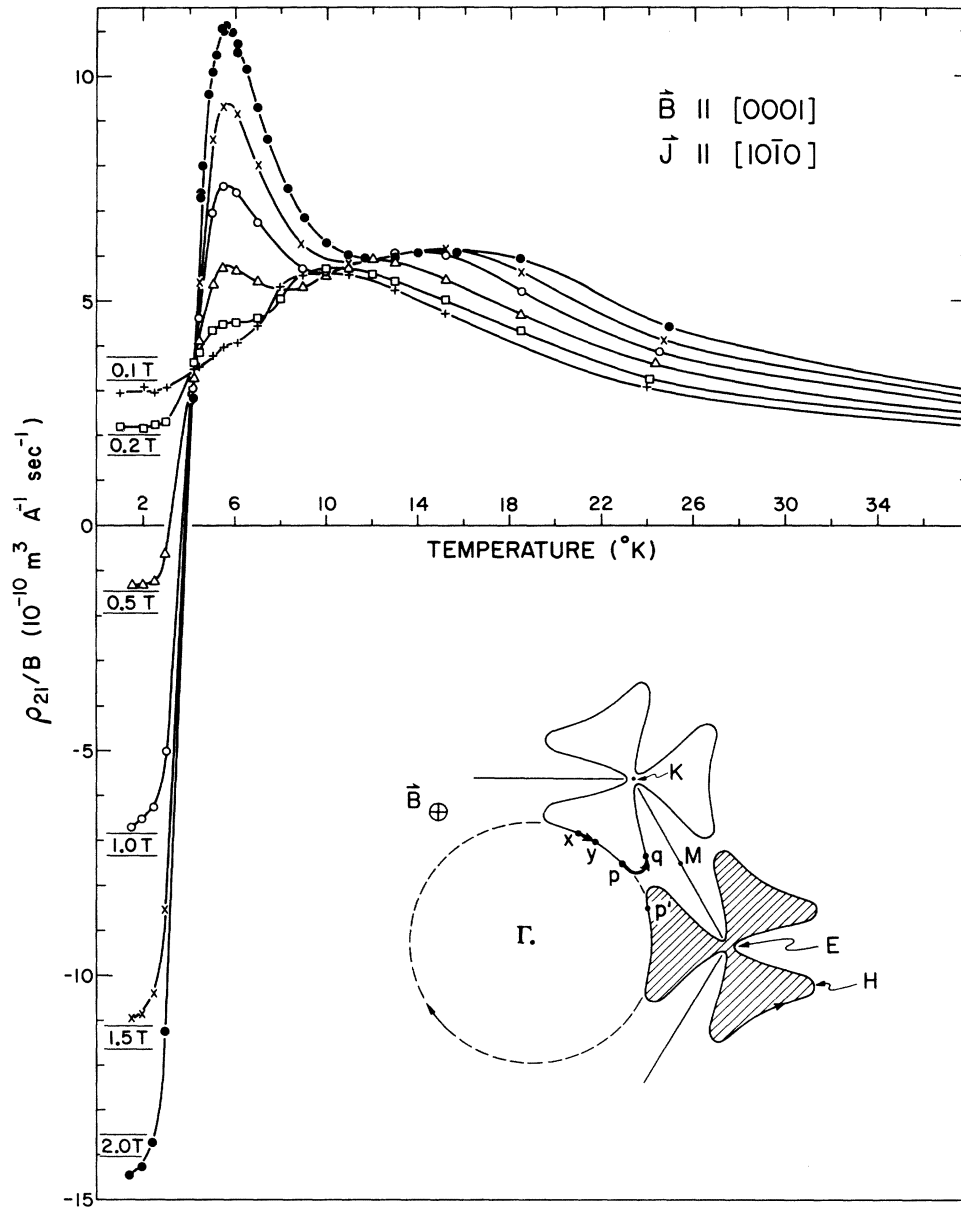
FIG. 2. Enlarged view of part of the behavior shown in Fig. 1. Exactly the same circumstances prevail except that here the effect of six different applied field strengths is shown. Insert: a section of the basal (ΓKM) plane of reciprocal space showing schematically the arrangement of the cloverleaf sections of the trifoliate surface. It is sufficient here to show two of these, but in a complete drawing of the extended zone scheme equivalent clover leaf sections would be located at the vertices of a space-filling array of hexagons.

sented on the trifoliate part of the reconstructed Fermi surface[1] (since the volume of reciprocal space occupied by the second-zone caps is small by comparison) and it is the behavior expected of electrons represented on such a surface which forms the pivot of our description. A typical cross section of this trifoliate part, here taken in the basal plane (ΓKM) of the Brillouin zone, is shown shaded in the insert of Fig. 2. Before turn-

ing to our model of this surface, it will perhaps be helpful to make a few general remarks about the orbits it can support.

We recall that in any plane perpendicular to an applied field $\vec{B}$ the effect is to move the representative points around the cyclotron orbit. If the dynamical low-field condition prevails for the orbit (i.e., if $\omega\tau \ll 1$ in the usual nomenclature[4]), then during the electron's mean free lifetime the
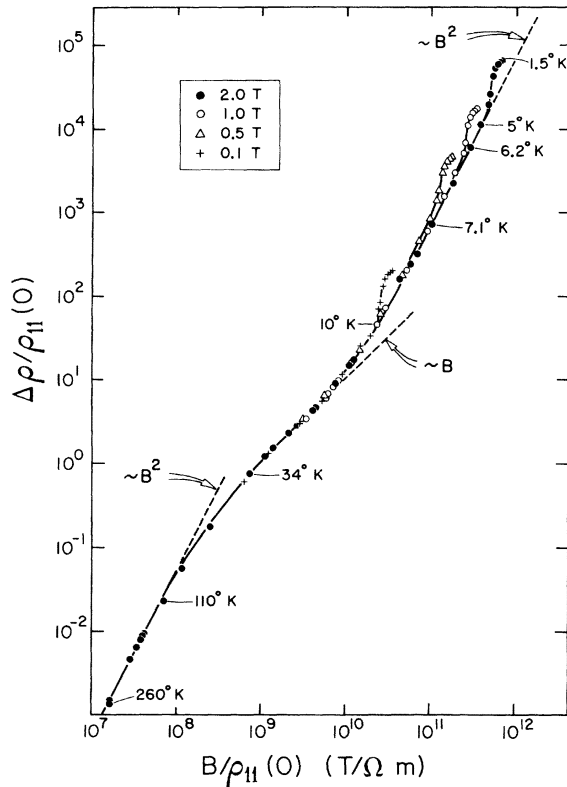
FIG. 3. Kohler plot showing the variation of the total transverse magnetoresistance $\Delta\rho = \rho_{11}(\vec{B}, T) - \rho_{11}(0, T)$ with field and temperature. Since it is impracticable to label each point with its temperature of measurement, the few chosen are some of those obtained at 2.0 T since these data form the basis of the arguments in Sec. VI.

representative point is able to complete only a short segment of the total orbit (such as $x \to y$ or $p \to q$ in Fig. 2). In the high-field condition ($\omega\tau \gg 1$), on the other hand, the representative point will complete many full cyclotron revolutions during the electron's lifetime (as around the entire perimeter of the shaded area in Fig. 2). Frequently the experimental circumstances are such that cyclotron orbits in both the high- and low-field conditions coexist on different planes drawn through the Fermi surface perpendicular to $\vec{B}$, and we shall call this the intermediate-field condition for the experiment. For an orbit like that shaded in Fig. 2, the net curvature of the completed segment of the orbit is of vital significance to the electron's overall response in the applied field. For example, in Fig. 2 the segment $p \to q$ includes a section having a curvature such that the electron's net rotation about $\vec{B}$ is in the direction expected from a positively charged particle, while the segment $x \to y$ is to a first approximation equivalent to part of the orbit of a free electron of

equivalent energy (shown dashed), and so the electron represented by this segment will during its lifetime have the usual response expected from a negatively charged particle.

Consequently, in the low- and intermediate-field conditions a hole surface like that of Fig. 2 can support orbital segments of both electronlike and holelike character. Both types contribute to the conduction parallel to the basal plane, and the Hall effect (which is odd in the sign of the charge carrier) reflects the balance between their contributions when summed over all planes perpendicular to $\vec{B}$. A change produced in the mean length of the segment traced out on such an orbit will generally alter the relative amounts of electronlike and holelike response, and so will be manifested in the Hall effect. For example, suppose that the effect of a change in the mean relaxation time of an orbit is to extend a segment like $x \to y$ into one say $x \to q$; then the net response of the electron will be changed from electronlike to holelike. (The second-zone hole surface in Al provides a prominent example of this mechanism; it dominates the metal's Hall effect, which consequently switches from electronlike in the low-field condition to holelike in the high-field one. Forsvoll and Holwech[10] first pointed out this interpretation, while Böning et al.[11] and Douglas and Datars[12] have since elaborated upon it.)

To accommodate these features in a semiclassical path-integral calculation of the galvanomagnetic tensor, we have used a single, cylindrical sheet of Fermi surface having the cross section shown in Fig. 4. As we pointed out in Sec. I, in this par-
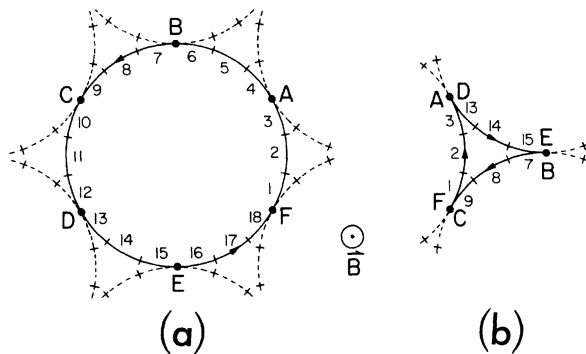

FIG. 4. Section through the sheet of cylindrical Fermi surface that is used in the path-integral calculation of the resistivity tensor. Here we show the section in the basal plane ΓKM of the Brillouin zone. The solid lines represent in (a) the giant cyclotron orbit available to an electron able to undergo scattering between the orbit's pieces at the points $A, B, \ldots, F$. In (b) the solid line represents the hole orbit produced where interpiece scattering is not permitted, corresponding to the cloverleaf orbits of Fig. 2.

ticular case, where the electron motion is confined to the basal plane, a single hole sheet is
sufficient to describe the electronic motion because the electrons on the lens are so ineffectual
in the total electron flux that they can be neglected.
The orbit shown in Fig. 4 is therefore used to imitate the dynamics of the electrons on the second-
zone monster hole surface whose cross section in
the basal plane is shown more realistically in Fig.
2. We shall see that three distinguishing features
of the trifoliate surface's cross section (shaded
in Fig. 2) must be possessed by the chosen model
before it can qualitatively imitate the observed
field and temperature dependences of the magneto-
resistive tensor. These features are electronlike
segments of moderate curvature (such as $x \to y$ in
Fig. 2), holelike segments of high curvature (as
$p \to q$ or that labeled H in Fig. 2), and electronlike
segments of high curvature (as that labeled E).
We see below that these features are sufficient to
give a qualitatively correct interpretation of the
observed magnetoresistive tensor, and it is not
necessary to have an exact geometrical replica of
the trifoliate cross section.

Following the method introduced by Falicov and
Sievert,[13] later modified by Young et al.[7] to include
intersheet scattering, we approximate the cyclotron orbit in the basal plane of the monster surface by six contiguous circular pieces (labeled
$AB, BC, \ldots$, in Fig. 4) each divided into three
arcs (numbered in Fig. 4). We assume explicitly
that magnetic breakdown does not occur in this
application (our maximum applied field is 2.0 T,
compared with 3.5 T at which breakdown in the
basal plane of Cd is first observed). Interpiece
scattering between channels[7] is permitted only at
the six points $A, B, \ldots, F$, corresponding to transitions like $p \to p'$ of Fig. 2. (We prefer the term
"interpiece" scattering when referring to the model of Fig. 4 since it emphasizes that the scattering is between pieces of an orbit on the single
sheet of the model Fermi surface.) These so-
called "hot spots" represent the initial and final
wave vectors of small-angle scattering processes
that happen to start and finish on different but adjacent areas of the Fermi surface. The probability
that an electron will make such an interpiece transition between any of these points is say Q, which
we take to be given by Young's two-channel expression[5]

$$Q = 1 - 0.5 \left[1 + \frac{e^x - 0.5\omega\Pi(1 - e^x)}{1 - 0.5\omega\Pi(1 - e^x)} \right]. \tag{1}$$

Here ω is the cyclotron frequency of the orbit in
question, and $x = -1/\omega\Pi$. This is a particularly
convenient characterization of the interpiece mechanism since it involves just a single parameter Π,

which is the typical scattering time for the two-
channel process. The corresponding probability
that an electron will undergo a Bragg reflection
at any of the six points $A, B, \ldots, F$, and so will
remain on its incident part of the Fermi surface,
is thus $1 - Q$ ($\equiv P$, the "interchannel scattering
probability"). The solid lines in Fig. 4 represent
the cyclotron orbits of an electron (a) with interpiece scattering (leading to a giant electronlike
orbit shown dotted in Fig. 2) and (b) without interpiece scattering (giving a hole orbit representing
the shaded trifoliate section in Fig. 2).

The effect of such interpiece scattering is included in the calculation[14] as a matrix $\underline{M}$, where
the element M_{xy} is the probability that an electron
which goes to the xth piece of cyclotron orbit will
have come from the yth. $\underline{M}$ is here the matrix

$$\underline{M} = \begin{bmatrix} 0 & 0 & P & 0 & 0 & Q \\ Q & 0 & 0 & P & 0 & 0 \\ 0 & Q & 0 & 0 & P & 0 \\ 0 & 0 & Q & 0 & 0 & P \\ P & 0 & 0 & Q & 0 & 0 \\ 0 & P & 0 & 0 & Q & 0 \end{bmatrix} \tag{2}$$

The need to divide each orbit piece into three
arcs (Fig. 4) arises in an attempt to overcome a
fundamental weakness of this free-electron approach to the evidently non-free-electron conduction in the basal plane of Cd. To see this weakness, consider the cyclotron orbit shown as a solid line in Fig. 4(b), which we recall is the case
with negligible interpiece scattering. In the high-
field condition this is a hole orbit, but in the low-
field condition it can support both electronlike and
holelike conduction responses depending on whether points such as AD, EB, etc., are traversed during the electron's lifetime between momentum-
changing collisions. The net low-field response
of the orbit is electronlike, however, because of
the overwhelming contribution from its free-electron pieces $F \to A$, $D \to E$, and $B \to C$ (just like
the second-zone hole surface of Al described
above.) This heuristic interpretation is confirmed
by path-integral calculations, although it hardly
seems worth repeating the details here.[12] Briefly,
an orbit like that in Fig. 4(b) [or that of Fig. 5(a)
in Ref. 7] has a negative element σ_{21} in the magnetoconductivity tensor when $\omega\tau \gg 1$; its only possible response in the high-field condition is thus that
of a hole orbit. But in the low-field condition,
when $\omega\tau \ll 1$, σ_{21} is positive, showing the orbit's
net electronlike response in that case. Hence the
response of an orbit like that of Fig. 4(b) changes

monotonically from holelike to electronlike as $\omega\tau$ is varied over the appropriate range, and this is exactly what we see reflected in the Hall effect of Al. Since the low-field response of the orbit in Fig. 4(b) is electronlike, it means that, without further modification, the entire model shown in Fig. 4 is inapplicable to this case of Cd because we know from Fig. 1 that, in the absence of appreciable interpiece scattering, the basal-plane conduction is holelike over the whole temperature range up to the melting point.

We can overcome this difficulty by introducing (after Douglas and Datars[15]) a relaxation-time anisotropy into the path-integral calculation. Hence we need to divide each orbit piece in Fig. 4 into three arcs, for the Appendix describes how an arc-dependent electron relaxation time is introduced through the expression $\tau(\vec{k}) \equiv b_p\tau$, where b_p is the anisotropy coefficient for the pth arc and τ is a parameter that characterizes the relaxation time for the orbit. It is shown in the Appendix that b_p is related to a parameter a_p, which characterizes the radius of curvature of the pth arc in $\vec{k}$ space, by $a_p/b_p = c_p$. (Douglas and Datars[12] have called c_p the "transport anisotropy" parameter. Throughout the present work it was fixed at unity for all arcs.) We can increase or diminish the contribution of the pth arc to the magnetoconductivity tensor by choosing an appropriate b_p value (and hence a_p value since $c_p = 1$) and by a suitable choice of the arc's initial and final azimuth phase angles (α_p and β_p of the Appendix). By making b_p on arcs 2, 8, and 14 of Fig. 4(b) very small relative to the rest, and by increasing the phase angle ($\beta_p - \alpha_p$) of these arcs at the expense of their contiguous neighbors, we restrict the contributions of these electronlike segments and so render the orbit's response more holelike in the low-field condition. In this way we are able to diminish the free-electron-like response of the unrestricted orbit—even to the point of producing a holelike response from the orbit in the low-field condition—and so make the model more appropriate to the case under consideration.

This same contrivance has a second effect. By making b_p very small on arcs like 2, 8, and 14 of Fig. 4(b) we have made the effective curvature of these arcs correspondingly larger than the rest (since c_p is unity throughout). Thus we effectively introduce into Fig. 4(b) the remaining of the essential features described above: the high-curvature electronlike segments corresponding to E in Fig. 2. Figure 4 is therefore a picture of the orbit in γ space (of the Appendix), but in ordinary $\vec{k}$ space it would show different curvatures for arcs having different a_p values. With b_p (and hence a_p) chosen in the above fashion, the orbit of Fig.

4(b) has not only the potential to be holelike in the low-field condition, it has in addition the three essential features described above. Thus arcs 1, 3, 13, 15, 7, and 9 represent the electronlike segments of modest curvature, arcs 2, 8, and 14 represent the electronlike segments of high curvature, and the cusps AD, EB, and FC represent the holelike segments of high curvature.

IV. MODEL RESULTS AND DISCUSSION FOR PURE Cd

All the calculations are made with the model of Fig. 4 using an azimuth angle ($\beta - \alpha$ of Fig. 11) of 58° for arcs 2, 5, 8, ..., 17, and 1° for the rest. The relaxation-time anisotropy b_p assigned to arcs $p = 2, 5, 8, \ldots, 17$ is specified in the following for each case considered, but for the rest of the arcs it is fixed throughout at unity. We recall that the transport anisotropy parameter c_p (Appendix) is also fixed at unity for all arcs $p = 1, 2, \ldots, 18$. The only other variables in the calculation are two temperature-dependent quantities: the interpiece scattering time Π, which leads to the interpiece scattering probability through Eq. (1), and the characteristic relaxation time for the orbit τ, which specifies the local arc-dependent quantity $\tau(\vec{k})$ $= b_p\tau$. For the former we have used throughout the values given in Fig. 5, where Π varies mono-
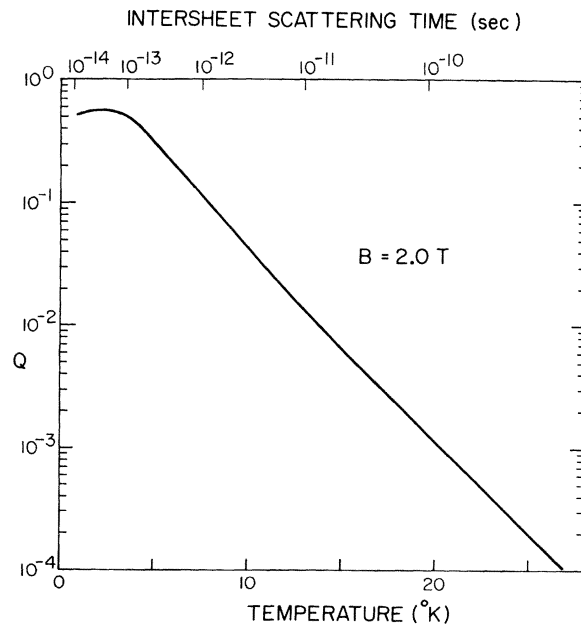
INTERSHEET SCATTERING TIME (sec)

FIG. 5. Temperature dependence of the Young *et al.* "intersheet scattering time" [Π of Eq. (1)] that is used throughout to describe the probability of scattering between pieces of the orbit in Fig. 4. The figure also shows the corresponding values of Q of Eq. (1) obtained in an applied field of 2.0 T.

tonically between 1.3×10^{-14} sec at 1 °K and 1.7
$\times 10^{-9}$ sec at 30 °K. This arbitrary range was
chosen to match what is thought to be the physical
situation[7] where the interpiece scattering probabil-
ity is a maximum[16] at the lowest temperature
($Q = 0.52$ at 1 °K for $\vec{B} = 2.0$ T) and becomes neglig-
ible above about 20 °K ($Q \approx 1 \times 10^{-4}$ at 30 °K for $\vec{B}$
$= 2.0$ T). Figure 5 shows the full range of Q given
by Eq. (1) for $\vec{B} = 2.0$ T. Note that the mid-range
value of Q (corresponding to a 50% chance of inter-
piece scattering) occurs at about 6 °K for $\vec{B} = 2.0$ T.
For the temperature dependence of the relaxation
time τ, we have used the variation shown by curve
1 in Fig. 6. This is again a somewhat arbitrary
choice based upon what are thought to be realistic
assumptions. We follow previous practice[7] and
assume a relaxation time of the form $1/\tau = R + ST^n$,
where R and S are obtained from experimental
data. Taking Hambourger's result[17] that $n = 3$ for
an orbit on the monster, and using our previous
data for the resistivity for Cd monocrystals pre-
pared in identical circumstances,[18] leads to the
dependence $1/\tau = (8.68 + 0.45T^3) \times 10^9$ sec^{-1} shown
by curve 1 in Fig. 6.

Figures 7(a) and 7(b) compare the observed and
calculated temperature dependences of the Hall
resistivity for the illustrative cases when $\vec{B} = 2.0$
and 0.1 T. (The corresponding behaviors found
for other field strengths in this range vary syste-
matically between the cases illustrated and seem-

FIG. 7. Comparison of the measured and calculated
$\rho_{21}(T)$ for pure Cd in the applied fields shown (a) Ex-
perimental data from Fig. 2; (b) corresponding results
from the calculation outlined in Sec. IV. The variations
A, B, and C correspond to the choices of b_p (T) labeled
in Fig. 8 and illustrate the sensitivity of the calculation
to a small change in the anisotropy of the relaxation
time. (c) The effect of varying the interpiece scatter-
ing when $\vec{B} = 2.0$ T. Curves 1 → 4 represent increasing
interpiece scattering, while curve 5 shows the behavior
when the scattering is turned off.

ingly do not warrant special consideration.) In
addition to the temperature-dependent Π and τ
values defined in Figs. 5 and 6 (curve 1), respec-
tively, the calculation also uses the temperature-
dependent anisotropy b_p ($p = 2, 5, 8, \ldots, 17$) shown
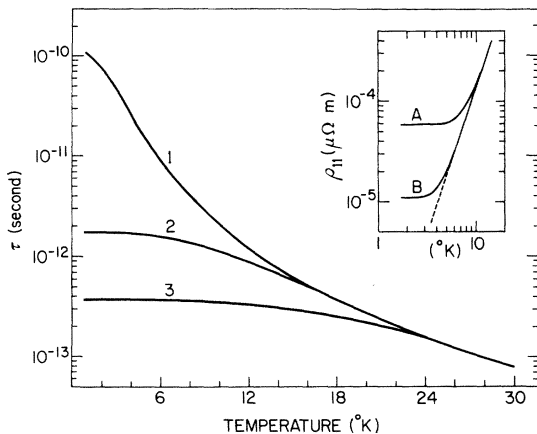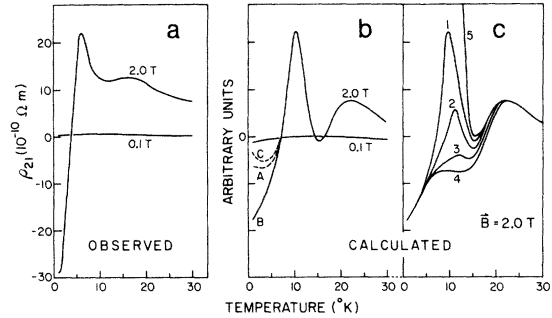in Fig. 8. The gross range of this parameter is

FIG. 6. Temperature dependence $\tau(T)$ of the average
relaxation time around the orbit of Fig. 4 that is used
in the calculations. Curve 1 is the form used for pure
Cd, where $1/\tau = R + ST^3$ as described in the text. Curves
2 and 3 are the forms used in the calculations for the
alloys described in Sec. V. It is described how their
choice is based upon the observed $\rho_{11}(T)$ shown in the
insert. Curve A is the observed $\rho_{11}(T)$ for Cd + 330-at.-
ppm Zn and B is that for Cd + 93-at.-ppm Zn. Corres-
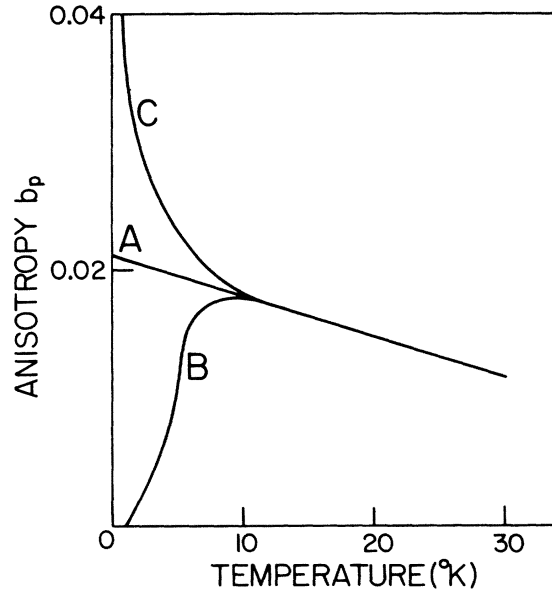ponding values for pure Cd are given in Ref. 18.

FIG. 8. Temperature dependence of the anisotropy
parameter b_p [where $\tau(\vec{k}) = b_p \tau; p = 2, 5, 8, \ldots, 17$] used
throughout the calculations. The curves A, B, and C
are alternative behaviors that are chosen to represent
the transition from an impurity-dominated to a phonon-
dominated range of temperature.

chosen to reduce sufficiently the free-electron con-
tributions of the orbit (Sec. III), so that its low-
field response in the temperature range of interest
is holelike, while the proposed variation of b_p with
temperature is designed to represent the division
between the phonon-dominated and impurity-dom-
inated ranges. Thus as the temperature is re-
duced from 30 °K, we let b_p increase to simulate
the lengthening lifetimes on arcs 2, 5, 8, . . . , 17
(Fig. 4) as the umklapp processes originating on
them are cut off because of the elimination of the
higher-energy phonons in the energy spectrum.
(This mechanism, first proposed by Ziman[19] in
connection with the "belly" areas of the group-IB
metals, is believed to have an important influence
on the Hall effect of many metals[20] in the approxi-
mate range 10–70 °K.) Ultimately, however, a
temperature is reached (about 6 °K in this case[21])
below which the scattering is increasingly influ-
enced by the residual impurity with its particular
and unknown anisotropy. To simulate this, and to
illustrate the sensitivity of the calculation to the
anisotropy parameter, we have considered separ-
ately the three dependences shown in Fig. 8. The
influence of these alternatives is shown for $\vec{B}$
= 2.0 T in Fig. 7(b). (A corresponding but less
prominent behavior is also found for $\vec{B}$ = 0.1 T,
although not shown.) The curves A, B, and C
correspond to the choices of $b_p(T)$ so-labelled in
Fig. 8. Clearly, the low-temperature results
from the model are quite sensitive to the aniso-
tropy parameter—a realistic feature that reflects
the known sensitivity of ρ_{21} to traces of different
impurity[2,4]—and give best agreement with experi-
ment when the form B of Fig. 8 is used to describe
the impurity-dominated range.

Assuming for $b_p(T)$ the behavior B of Fig. 8
leads to the results shown as solid lines in Fig.
7(b). These replicate—qualitatively, at least—
the gross features observed experimentally over
the same temperature range [Fig. 7(a)]. In high-
er applied fields $\rho_{21}(T)$ shows two local positive
maxima centered at about 10 and 20 °K, and a
sharp transition to negative values as the lowest
temperatures are approached. As the field
strength is reduced, these features become in-
creasingly insignificant, and have disappeared
for $\vec{B}$ = 0.1 T. The most striking discrepancies
with experiment are the pronounced dip to nega-
tive values at about 15 °K ($\vec{B}$ = 2.0 T), and the nega-
tive sign calculated for ρ_{21} over most of the tem-
perature range in the lower applied field [Fig.
7(b)]. Both of these discrepancies stem from the
inherent free-electron nature of the unrestricted
orbit of Fig. 4(b), already referred to in Sec. III.
Further juggling of the chosen b_p and azimuth
angles subtended by arcs p = 2, 5, 8, . . . , 17 could

undoubtedly reduce these discrepancies, but it
hardly seems worth the cost of further computa-
tion with such a basically crude model. As it
stands it is adequate for our purpose, which is
to derive a qualitative interpretation of the data
shown in Figs. 1 and 2.

Consider the $\rho_{21}(T)$ shown in Fig. 7(b) for $\vec{B}$
= 2.0 T. We recall that at the highest tempera-
tures the calculation permits essentially no inter-
sheet scattering, so the orbit of Fig. 4(b) is there-
fore the appropriate description. As the tempera-
ture is reduced from 30 °K, there is a shift to-
wards the more holelike response that an orbit
like Fig. 4(b) shows as its effective value of $\omega\tau$
increases (as described in Sec. III). For a con-
tinuing reduction in temperature, however, the
chosen $b_p(T)$ (Fig. 6) eventually produces the re-
verse tendency. Our calculations suggest that it
is the high-curvature electron segments we have
created on arcs like 2, 8, and 14 of Fig. 4(b) that
are important in producing this feature. This
electronlike tendency becomes dominant below a
sufficiently low temperature (~22 °K) and $\rho_{21}(T)$
then begins a marked tendency towards more nega-
tive values. This would continue as $\omega\tau$ is in-
creased if it were not that ultimately the entire
orbit must enter the high-field regime, and there
its response can only be (Sec. III) that of a hole
orbit. [The effective $\omega\tau$ values when $\vec{B}$ = 2.0 T
for the orbit of Fig. 4(b) are typically 77 at 1 °K,
2.9 at 8 °K, 0.9 at 12 °K, and 0.06 at 30 °K; the
corresponding value of $\omega\tau$ for the giant electron
orbit of Fig. 4(a) at a given temperature is ap-
proximately half that for the orbit of Fig. 4(b).]

Superimposed upon these features is the effect
of the interpiece scattering. This can be judged
from Fig. 7(c), which shows for $\vec{B}$ = 2.0 T the re-
sults of varying amounts of such scattering.
Curve 1, which is reproduced from Fig. 7(b), is
the result obtained with $\Pi(T)$ given by Fig. 5, $\tau(T)$
given by curve 1 of Fig. 6, and b_p given by curve
B of Fig. 8. Curves 2, 3, and 4 correspond to
the same conditions except that the interpiece
scattering time is taken to be, respectively,
$\Pi(T)/2$, $\Pi(T)/4$, and $\Pi(T)/10$; thus curves 1 → 4
correspond to increasing interpiece scattering at
any temperature. The effect of such an increase
is clearly to decrease the high-field contribution
from the hole orbit of Fig. 4(b): Increasing inter-
piece scattering means an increasing contribution
from the giant electron orbit of Fig. 4(a) at the ex-
pense of the alternative in Fig. 4(b), and the con-
tinuing reduction in temperature takes the giant
orbit itself towards its high-field limit. [Hence
the sharp swing to negative values of $\rho_{21}(T)$ pro-
duced by the interpiece scattering.[7]] Finally,
curve 5 is the result when the interpiece scatter-

ing is turned off completely for all temperatures (Q is set to zero in the matrix $\underline{M}$ of Sec. III). The local maximum at about 20 °K is not affected—as is expected since the interpiece scattering plays no part in its origin—but the transition to the high-field condition is now clearly delineated since the competing electron contribution from the giant orbit of Fig. 4(a) has been removed.

V. MODEL RESULTS AND DISCUSSION FOR CdZn

Although we have not attempted a systematic study of the effects of different solutes, it is worth noting the results shown in Fig. 9 for Cd containing Zn, since they provide a further indirect test of the above model and its interpretation. Curve 1 of Fig. 9(a) is the behavior of $\rho_{21}(T)$ measured in pure Cd when $\vec{B}=2.0$ T [as in Fig. 7(a)]; curves 2 and 3 are, respectively, the corresponding behaviors measured for alloys containing 350- and 93-at.-ppm Zn. Figure 9(b) shows how the model described in Sec. IV can reproduce these effects. Curve 1, which is repeated from Fig. 7(b), is the result obtained for pure Cd using the parameters defined in Sec. IV [in particular, the $\tau(T)$ used for this case is the variation 1 of Fig. 6]. Curves 2 and 3 of Fig. 9(b) are the results obtained from an identical calculation except that the $\tau(T)$ is now replaced by the variations 2 and 3 of Fig. 6, respectively. [These $\tau(T)$ variations are chosen in the following way: $\tau(1.7$ °K) for each alloy is determined from the ratio $\tau(Cd)/\tau(alloy)=\rho_{11}(alloy)/\rho_{11}(Cd)$, using the data shown in the insert to Fig. 6. The extent of the temperature-independent range of $\tau(T)$ is read directly off the $\rho_{11}(T)$ curve, and its upper end is then joined by a smooth curve to the background phonon variation.]

Figure 9 shows that, using a plausible $\tau(T)$, the model can reproduce the qualitative features observed experimentally for $\rho_{21}(T)$ when the solute is added. Since the applied field is kept fixed, any solute addition shifts the theoretical condition for a given temperature away from the high-field limit. Consequently, the high-field contributions from both the hole orbit [Fig. 4(b)] and the giant electron orbit [Fig. 4(a)] are reduced, which means that both the local maximum in $\rho_{21}(T)$ seen at about 10 °K, and the strongly negative tendency seen at the lower temperatures, are reduced by the solute. A sufficient addition renders $\rho_{21}(T)$ to a behavior not unlike that observed for pure Cd in the lowest applied fields, where vestiges of high-field behavior are of course suppressed.

Two discordant features seen between the observed and calculated $\rho_{21}(T)$ for the most-concentrated alloy (curves 3 of Fig. 9) deserve comment. The first is that in the approximate range 14–22 °K
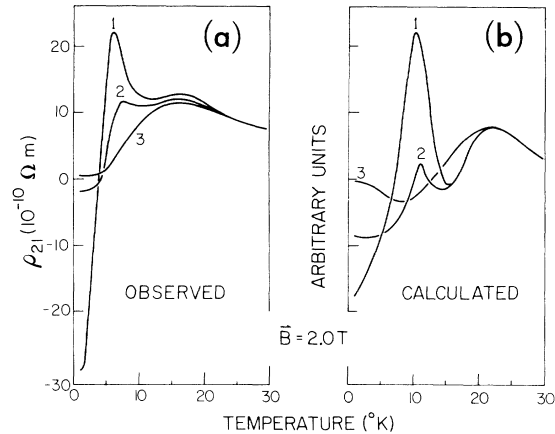

FIG. 9. Comparison of the (a) observed and (b) calculated $\rho_{21}(T)$ at $\vec{B}=2.0$ T for Cd (curve 1) and Cd containing mean values of 93- and 330-at.-ppm Zn (curves 2 and 3, respectively). (Analyses of the top and bottom of each sample gave ranges of 87–98 and 310–349 at. ppm.) The orientations of $\vec{B}$ and $\vec{J}$ are as defined in Fig. 2. The residual-resistance ratios $(R_{273^\circ K}/R_{1.7^\circ K})$ of the samples are 25 600 (curve 1), 5780 (curve 2), and 1112 (curve 3). Identical parameters are used for the calculations shown in (b) except for the chosen $\tau(T)$ shown in Fig. 6.

the calculated $\rho_{21}(T)$ is more positive than either of the other less-concentrated cases. The second is the marked tendency of $\rho_{21}(T)$ to more positive values as the temperature is reduced below about 10 °K. Both of these details are connected with the particular anisotropy $b_p(T)$ assumed for the calculation. In Fig. 9(b) we have for simplicity let $b_p(T)$ be fixed throughout as the variation B of Fig. 8, but this assumption may be too gross since Zn could well have a distinctive scattering anisotropy that is quite different from that of the unknown dominant impurity in our pure Cd. The sensitivity of the calculations to this parameter has already been shown in Fig. 7(b), and no doubt improvements could be made to the calculations in Fig. 9(b) by introducing a different $b_p(T)$, but, just as in the case of difficulties discussed in Sec. IV, we feel that here the present model is adequate for our qualitative requirements.

VI. CONCLUSIONS

Figure 10 shows schematically the salient features of $\rho_{21}(T)$ observed for Cd in the temperature range below about 30 °K. The solid line AF represents what can be called the low-field or background behavior seen when essentially none of the contributing orbits are in the high-field condition. (This is typically that of Figs. 1 and 2 when $\vec{B}$ $=0.1$ T.) Superimposed upon this background are
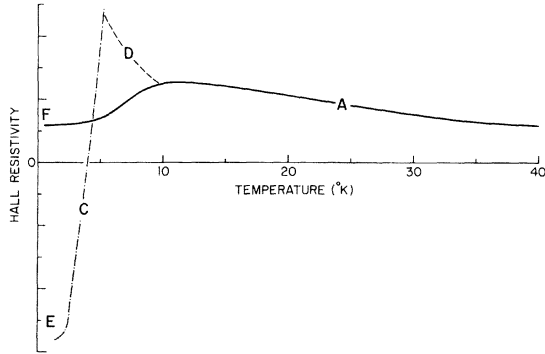
FIG. 10. Schematic diagram showing the salient features in the temperature dependence of $\rho_{21}(T)$ seen in the temperature range of Fig. 2. Curve AF represents the background or low-field dependence (as when $\vec{B}$ = 0.1 T in Fig. 2), while superimposed upon this are singular features, like C and D, which arise when particular topological features manifest themselves in the high-field conditions (as when $\vec{B}$ = 2.0 T in Fig. 2). At E we have the closest approach to the high-field limit possible in the experimental circumstances.

singular features that arise from contributing cyclotron orbits rendered to the high-field condition during the experiment. We turn first to the low-field behavior AF.

As the temperature is reduced below about 100 °K the conduction is at first increasingly dominated by holelike carriers (a feature that is most pronounced below about 50 °K). It has been suggested[19,20] that this pronounced feature (which is also seen in other metals[20]) arises from the "freezing out" of wide-angle scattering events from umklapp processes as the higher-energy lattice vibrations are extinguished. Support for this suggestion in the present context comes from the temperature dependence of the electrical resistance in zero applied field, $\rho_{11}(0, T)$, which shows a linear behavior down to about 50 °K. Below this temperature[21] there is a clear shift towards the usual T^5 dependence, indicating the beginning of the Bloch regime as the higher-energy phonons are frozen out. This temperature is seen (Fig. 1) to coincide closely with the onset of the tendency towards increasingly holelike behavior shown by $\rho_{21}(T)$. But it is not evident from the free-electron model of Secs. IV and V why this initial tendency in Cd should be towards more holelike behavior, for one would expect a preferential lengthening of the relaxation time to occur first on segments of the Fermi surface that are furthest removed from Brillouin-zone boundaries, and

these are just the most free-electron-like parts of the surface (like the regions covered by $x \rightarrow y$ in Fig. 2). Whatever its physical origin, however, this positive tendency is overcome by a tendency towards electronlike behavior as the temperature is reduced, and the result is a localized maximum in $\rho_{21}(T)$ at about 15 °K (AF of Fig. 10). Judging from the calculations described in Fig. 7(c), interpiece scattering does not figure prominently in forming this particular feature, although it may reinforce the tendency towards more negative $\rho_{21}(T)$ seen at the lowest temperatures even in the low-field data. (We have described in Sec. IV how in the model calculations the tendency to electronlike behavior is produced by a judicious choice of parameters that emphasises the contributions from segments like E in Fig. 2.)

The singular features that appear superimposed upon this low-field behavior when the applied field strength is increased sufficiently are of course most pronounced in the data obtained at 2.0 T (Figs. 1 and 2), which we therefore use for illustration (Fig. 10). Our suggestion is that these features (D and C of Fig. 10) are simply the high-field manifestation of two competing mechanisms already outlined. Thus D, the sudden upswing towards a marked domination by holelike carriers, arises when $\omega\tau$ for the clover-leaf orbit (i.e., around the shaded area of Fig. 2) approaches unity. (We described in Sec. IV how in the model calculations $\omega\tau$ for this orbit passes through unity in the interval between 8 and 12 °K.) When this is so, any completed segment on the orbit is long enough so that inevitably several of the clover leaf's tips (H of Fig. 2) are traversed during the electron's lifetime, so that the contribution to σ_{ij} from the orbit's strongly electronlike segments (E of Fig. 2) are outweighed. In other words, as the temperature is reduced and the completed orbital segment is continuously lengthened, short electronlike segments like $x \rightarrow y$ in Fig. 2 become very improbable in these circumstances; longer segments, which encompass several tips of the clover leaf and are therefore holelike, inevitably prevail as the high-field limit is approached. This qualitative argument is supported by the field dependence observed for the transverse magnetoresistance (Fig. 3). At 2.0 T in the temperature range down to about 34 °K the magnetoresistance shows the quadratic field dependence associated with the low-field condition. Then in the approximate range 11–34 °K it shows a roughly linear field dependence as it passes through the intermediate-field region, and finally reverts below about 10.5 °K to the quadratic dependence. This last behavior indicates[7] the onset of the prevailing high-field condition for this compensated metal

(which has only closed cyclotron orbits in this circumstance; the breakaway from this quadratic behavior below about $5.5\,°K$ seen in Fig. 3 is a separate effect connected with the high-field appearance of interpiece scattering that is discussed below). Reference to Fig. 2 shows that when $\vec{B} = 2.0$ T, $10.5\,°K$ coincides closely with the onset of what we propose is the high-field contribution from the trifoliate surface. Thus our argument is supported by the separate and empirical criterion for high-field behavior which the magnetoresistance provides. Furthermore, when the same comparison is made between the data of Figs. 2 and 3 obtained at other field strengths (viz., $0.2-1.5$ T), the same agreement is found; that is, the onset of the high-field condition indicated by Fig. 3 occurs in each case[22] at a temperature close to that seen in Fig. 2 which marks the swing to pronounced hole-like behavior.

Finally, there remains the feature C of Fig. 10. This behavior is the manifestation of the "intersheet scattering" in the high-field condition, as previous authors have already emphasized.[2-7] Briefly, as the clover-leaf orbit in a given plane perpendicular to $\vec{B}$ is rendered to the high-field condition so that a representative point makes numerous complete revolutions of it in the electron's lifetime, so those points which choose the alternative channel (like $p \to p'$ in Fig. 2) will be able to traverse an equivalent path length along their essentially free-electron orbit formed as shown dotted in Fig. 2. Thus as $\omega\tau$ for the clover-leaf orbit is increased, so eventually the high-field condition will be reached for this giant free-electron orbit. (For this to happen obviously requires a minimum $\omega\tau$ value sufficient to produce at least two complete revolutions for the clover-leaf orbit in the electron's lifetime, since one complete revolution of the dotted orbit requires about six traverses of a leaf's "face."[23]) Once the giant orbit attains the high-field condition its contribution is equivalent to that of a fictitious electron surface, and the metal's compensation in the plane is destroyed. Hence the marked swing towards electron-dominated behavior in the Hall effect[2-7] (C of Fig. 10), and the sharp breakdown of Kohler's rule (Fig. 3). As the temperature is reduced at a fixed field, this tendency seen in the Hall effect is maintained as long as $\omega\tau$ continues to increase and the conditions continue to approach the high-field limit. But eventually the residual-resistance range is reached and there the balance between holelike and electronlike contributions tends to a temperature-independent value (E of Fig. 10).

It should be noted that where we refer to the prevailing field condition in an experiment we

have tried to avoid recourse to values of $\omega\tau$ calculated from free-electron theory. (This contrasts with other approaches which have been made.[4-6]) For a metal like Cd, we maintain that such numbers, if they are not completely irrelevant, are at best misleading. The appropriate test for a prevailing condition in a galvanomagnetic effect is an empirical one, such as the behavior of the magnetoresistance (Fig. 3) or of the Hall effect itself (Fig. 2). For example, in a applied field of 0.1 T and with a residual resistance ratio ($R_{273\,°K}/R_{4.2\,°K}$) of 18 500, the free-electron $\omega\tau$ value of the sample described in Fig. 2 becomes[2] greater than 1 for temperatures below about $7\,°K$. But obviously this is not a sufficiently sensitive criterion for high-field behavior, for there is no evidence at 0.1 T of any significant contributions from the high-field singular features, and in fact there is only slight evidence of them even when $\vec{B} = 0.2$ T (which at $4.2\,°K$ gives $\omega\tau = 13$).

We now turn to the implication of our interpretation for the behaviors of $\rho_{21}(\vec{B}, T)$ that had been reported[2-4] for Cd containing very small amounts of solute. In particular we shall consider the conclusion by Lilly and Gerritsen[4] that "intersheet scattering" cannot account for their observation that a concentration of Ag of In as low as a few parts per million by weight will render $\rho_{21}(T)$ to a positive, temperature-independent value at the lowest temperatures.

From the discussion of Secs. IV and V it is seen that the effect of progressively adding electron scattering sources such as foreign atoms, will be eventually to prevent the clover-leaf orbits from achieving the high-field condition in the circumstances of the experiment. In other words, the electron's mean free lifetime will be reduced to the point that the combinations of applied field and temperatures which are available will be insufficient to produce the feature D (and hence C, since a high-field trifoliate surface is a prerequisite for a high-field giant orbit) of Fig. 10. For a sufficiently high solute concentration, a behavior of the low-field type AF of Fig. 10 will therefore be observed. This is not to say that the addition of the solute has either inhibited or enhanced the amount of intersheet scattering.[2-4] It simply means that the high-field manifestation C of the scattering cannot be made evident during the experiment and we are left simply with its low-field manifestation, which is embodied in the behavior AF as explained in Sec. VI.

Since the low-field Hall effect is determined by a summation involving the electron's velocity, effective mass, and anisotropic relaxation time at every point on the Fermi surface, the actual posi-

tion of F will depend upon the scattering aniso-
tropy of the dominant scattering mechanism—here
presumed to be the solute. But providing the so-
lute concentration is small enough that effects
such as solute-solute interaction and lattice-pa-
rameter changes can be neglected, the low-tem-
perature Hall effect (as at F in Fig. 10) tends to
a value independent of concentration and tempera-
ture.[24]

Although the range of solute concentrations
studied by Gerritsen and his students[2,4] is not
wide enough to establish with certainty the con-
centration-independent value of F (Fig. 10) for
each of the solutes, it is clear from his data that
the most-concentrated alloys give the behavior
AF appropriate to the low-field condition. (How-
ever, it seems safe to predict from the observed
tendencies that the low-temperature value of ρ_{21}
will in fact be positive for the Cd-Ag, Cd-In, and
Cd-Zn systems.) This appearance of a constant
$\rho_{21}(T)$ at the lowest temperatures when a little
solute is added, which posed problems of inter-
pretation, is seen to be rather the expected be-
havior in terms of our foregoing arguments. In
fact some of the most dilute alloy samples (for
example, CdIn-9 or CdIn-4 of Ref. 4) show the
approach to this low-field behavior AF of Fig. 10
as the features C and D are progressively re-
duced. Since these features are competitive con-
tributions to $\rho_{21}(T)$, and since they are not neces-
sarily extinguished at the same rates as solute
is added, it is clear that the net behavior of $\rho_{21}(T)$
for extremely dilute samples is not necessarily a
monotonic dependence upon the solute concentra-
tion. For example, Lilly and Gerritsen[4] find for
a Cd-Ag series of alloys that upon the smallest
addition of Ag the temperature-independent value
of ρ_{21} is first sharply increased to a positive value
but then subsequently decreases as further solute
is added. (We would maintain that this decrease
is the approach to the concentration-independent
low-field value.) This is said to be incompatible
with intersheet scattering, but it is clearly possi-
ble in terms of our interpretation. If the effect of
the electron scattering by Ag is more pronounced
for the giant electron orbit than for the clover-
leaf ones, the feature C of Fig. 10 will initially
be extinguished more rapidly than D. Eventually
when enough solute is added, D will also be ex-
tinguished, but the net effect for the region F will
be the dependence upon solute concentration seen
by Lilly and Gerritsen. Indeed, this dependence
could turn out to be the normal behavior of $\rho_{21}(T)$
at low temperatures, for the range and spacing of
the different concentrations studied in the Cd-Zn
and Cd-In systems[2,7] are insufficient to rule out
with certainty this possibility.

APPENDIX

The path-integral calculations follow closely
the method already outlined by Douglas and
Datars[12] that, in turn, is based upon the matrix
approach of Falicov and Sievert.[13] At the heart
of the calculation is the fact that the magnetocon-
ductivity tensor σ_{ij} arising from a cyclotron orbit
divided into pieces in the manner of Fig. 4 can be
written in terms of certain integrals. The differ-
ential form of this is

$$\frac{d\sigma_{ij}(k_z)}{dk_z} = \frac{m_0 e^2}{4\pi^3 \hbar^2 \omega_0} \sum_{\text{all orbits}} \sum_{\text{all pieces}} B_q^i D_q^j + C_q^{ij},$$

(A1)

where σ_{ij} is defined with respect to a right-handed
set of axes having the applied field $\vec{B}$ along the z
direction, and dk_z is the thickness of the slice con-
taining the plane $k_z = \text{const}$ in which the orbit is
located in $\vec{k}$ space. B_q^i, D_q^j, and C_q^{ij} are the piece
integrals [Eqs. (2)–(4) of Ref. 15] of the qth piece.

Each orbit piece is divided into N circular arcs.
The general pth arc is specified by the following
six arc-dependent parameters[15] (refer to Fig. 11).
First, α_p and β_p are the initial and final values of
the geometrical azimuth variable γ over the arc.
For convenience, γ has replaced the phase vari-
able[15] θ in the standard expression for the conductivity
tensor[25]; thus $\theta = a_p \gamma$, where $a_p = \hbar k_\perp^p / m_0 v_\perp^p$. a_p is thus
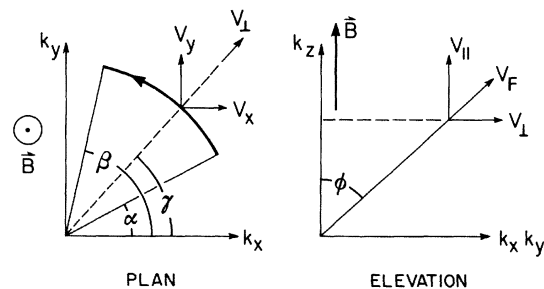related to the radius of curvature $k_\perp^p$ of the pth

FIG. 11. Geometrical parameters described in the
Appendix that are used to specify a general arc of a
circular cyclotron orbit in phase space. γ is the geome-
trical azimuth phase that varies between its initial and
final limits, α and β. ϕ is the colatitude angle, and is
$\pi/2$ in the case of our cylindrical Fermi surface. v_f is
the Fermi velocity.

arc in the plane $k_z = $ const of $\vec{k}$ space (Fig. 4). Second, $v_\perp^p$ and $v_\parallel^p$ denote, respectively, the components of the Fermi velocity that are perpendicular and parallel to the applied field's direction $\vec{B}$, with a similar convention for the electron's wave vector $\vec{k}$. Finally, b_p defines the anisotropy of the relaxation time from arc to arc. Thus $\tau(\vec{k})$ on the pth arc is τb_p, where τ is a parameter that characterizes the relaxation time for the orbit containing the arc. The ratio a_p/b_p is written c_p by Douglas and Datars[12] and is called the "transport anisotropy." Throughout the present work this ratio was fixed at unity for all arcs. Written in terms of these parameters, the 15 arc integrals for the pth arc are (where $i,j = x, y, z$)

$$A_p^i(\omega_0\tau) = a_p \int_{\alpha_p}^{\beta_p} d\gamma \, v_i(\gamma) \exp[(\gamma - \beta_p)c_p/\omega_0\tau],$$

(A2)

$$B_p^i(\omega_0\tau) = a_p \int_{\alpha_p}^{\beta_p} d\gamma \, v_i(\gamma) \exp[(\alpha_p - \gamma)c_p/\omega_0\tau],$$

(A3)

$$C_p^{ij}(\omega_0\tau) = a_p^2 \int_{\alpha_p}^{\beta_p} d\gamma \int_{\alpha_p}^{\gamma} d\gamma' \, v_i(\gamma)v_j(\gamma')$$
$$\times \exp[(\gamma' - \gamma)c_p/\omega_0\tau].$$

(A4)

Because the arc is circular, the evaluation of Eqs. (A2)–(A4) for any arc is straightforward. It is recalled from Fig. 11 that $v_x(\gamma) = v_\perp \cos\gamma$, $v_y = v_\perp \sin\gamma$, and $v_z(\gamma) = v_\parallel$. Substitution into Eqs. (A2)–(A4) reduces each of the 15 expressions to a standard analytical integral having a known solution.

The calculation takes the following steps. For the qth piece of the orbit [such as $A \to B$ in Fig. 4(a)], that is itself divided into N arcs, the $15 \times N$ arc integrals of Eqs. (A2)–(A4) are determined from their analytical forms. The corresponding piece integrals for this qth piece are then determined from the recursion relations[15] (where p is again the arc index, $p = 1, 2, \ldots, N$, and $\tilde{A}_p^i$, etc., implies the value of the quantity evaluated up to the end of the pth arc):

$$\tilde{A}_p^i = \tilde{A}_{p-1}^i \exp[-(\beta_p - \alpha_p)c_p/\omega_0\tau] + A_p^i,$$

(A5)

$$\tilde{B}_p^i = \tilde{B}_{p-1}^i + B_p^i \exp(-\phi_{p-1}'/\omega_0\tau),$$

(A6)

$$\tilde{C}_p^{ij} = \tilde{C}_{p-1}^{ij} + C_p^{ij} + B_p^i \tilde{A}_{p-1}^j,$$

(A7)

$$\phi_p' = \phi_{p-1}' + (\beta_p - \alpha_p)c_p.$$

(A8)

At this point the piece integrals A_q^i, B_q^i, and C_q^{ij} have been determined for the orbit piece in question. B_q^i and C_q^{ij} appear directly in the conductivity [Eq. (A1)] while A_q^i is required to calculate the remaining piece integral D_q^i in the conductivity. This integral accounts for the electron's previous history[12,15] before it arrived on the current piece of orbit, and so includes the interpiece scattering effects. It can be shown[13] that if the cyclotron orbit consists of n pieces then D_q^i is related to the piece integrals A_q^i by

$$
\begin{bmatrix} D_1^i \\ D_2^i \\ \vdots \\ D_q^i \\ \vdots \\ D_n^i \end{bmatrix} = (\underline{I} - \underline{ME})^{-1}\underline{M} \begin{bmatrix} A_1^i \\ A_2^i \\ \vdots \\ A_q^i \\ \vdots \\ A_n^i \end{bmatrix},
$$

(A9)

where $\underline{I}$, $\underline{M}$, and $\underline{E}$ (which are all $n \times n$ matrices) are, respectively, the identity matrix, the interpiece transition probability matrix (defined in Sec. III), and the diagonal matrix having elements

$$E_{qr} = \delta_{qr} \exp(-\phi_q'/\omega_0\tau)$$

$$\equiv \delta_{qr} \exp\left(\sum_1^N - \frac{(\beta_p - \alpha_p)c_p}{\omega_0\tau}\right).$$

(A10)

With B_q^i, D_q^i, and C_q^{ij} evaluated for each piece, the summation of $(B_q^i D_q^j + C_q^{ij})$ for all n pieces around the orbit is taken [Eq. (A1)] to give the orbit's contributions to the nine components of the differential conductivity. If there are other contributing orbits in the same plane $k_z = $ const, then the process must be repeated and the summation made over the whole plane. Finally, unless the Fermi surface is cylindrical and has its axis collinear with $\vec{B}$ (so that the colatitude angle $\phi = \pi/2$ in Fig. 11—as it was throughout our calculations), the process must be repeated and summed over all appropriate planes $k_z = $ const in the Brillouin zone. The accumulated magnetoconductive tensor is then inverted to give the magnetoresistive tensor.

---

[1] D. C. Tsui and R. W. Stark, Phys. Rev. Lett. **16**, 19 (1966); J. K. Galt, F. R. Merritt, and J. R. Klauder, Phys. Rev. **139**, A823 (1965).

[2] O. P. Katyal and A. N. Gerritsen, Phys. Rev. **178**, 1037 (1969).

[3] H. Schwarz, Phys. Status Solidi **39**, 515 (1970).

[4] D. A. Lilly and A. N. Gerritsen, Phys. Rev. B **9**, 2497 (1974); Physica **69**, 286 (1973); A. N. Gerritsen, Phys.

Rev. B 10, 5232 (1974); 12, 4247 (1975).

[5] R. A. Young, Phys. Rev. 175, 813 (1968).

[6] O. P. Katyal, A. N. Gerritsen, J. Ruvalds, R. A. Young, and L. M. Falicov, Phys. Rev. Lett. 21, 694 (1968).

[7] R. A. Young, J. Ruvalds, and L. M. Falicov, Phys. Rev. 178, 1043 (1969).

[8] C. M. Hurd and J. E. A. Alderson, J. Phys. Chem. Solids 32, 175 (1971); 33, 767 (1972).

[9] J. E. A. Alderson, T. Farrell, and C. M. Hurd, Phys. Rev. 174, 729 (1968).

[10] K. Forsvoll and I. Holwech, Philos. Mag. 10, 921 (1964).

[11] K. Böning, H. J. Fenzl, J. M. Welter, and H. Wenzl, Phys. Status Solidi 40, 609 (1970).

[12] R. J. Douglas and W. R. Datars, Can. J. Phys. 51, 1770 (1973).

[13] L. M. Falicov and P. R. Sievert, Phys. Rev. 138, A88 (1965).

[14] It is perhaps worth noting that Eq. (2.11) in Ref. 7 is misprinted. The correct version is

$$M = \begin{bmatrix} O & Q & O & P \\ P & O & Q & O \\ O & P & O & Q \\ Q & O & P & O \end{bmatrix}$$

By recalculating a couple of the cases discussed in that paper, we have confirmed that the correct form of the matrix must have been used in the original calculations. We are indebted to R. A. Young for useful correspondence on this point.

[15] R. J. Douglas and W. R. Datars, Can. J. Phys. 53, 1060 (1975). This paper contains typographical errors that could be misleading. Important ones in the present context occur in their recursion relations [A4]–[A7]. Datars kindly showed us listings of the programs used by his group and we see from these that the correct forms (given in the Appendix) were used in Douglas and Datars's calculations.

[16] Figure 2 of Ref. 7 shows the variations of P and Q between their limiting values.

[17] P. D. Hambourger, in *Proceedings of the 13th International Low Temperature Physics Conference, Boulder, Colorado, 1972,* edited by R. H. Kropschot and K. D. Timmerhaus (University of Colorado, Boulder, Colo., 1973), p. 278.

[18] J. E. A. Alderson and C. M. Hurd, Phys. Rev. B 12, 501 (1975).

[19] J. M. Ziman, Phys. Rev. 121, 1320 (1961).

[20] C. M. Hurd, *Hall Effect in Metals and Alloys* (Plenum, New York, 1972), Chap. 3.

[21] J. E. A. Alderson (unpublished).

[22] This statement cannot be verified from Fig. 3 as it is reproduced here since only the temperatures corresponding to $\vec{B} = 2.0$ T are shown. However, the full set of tabulated data is available upon request.

[23] It is important to bear in mind that the Hall effect is not a quantum effect. Unlike the the de Haas–van Alphen effect, for example, it does not require a strict quantum phase coherence to be maintained around a high-field orbit. This means that a low-angle scattering process which simply displaces the representative point along the same orbit does not destroy the orbit's high-field contribution to the Hall effect [A. B. Pippard, Proc. R. Soc. A 305, 291 (1968)]. So the "high-field" requirement for a classical galvanomagnetic effect is less stringent than for a quantum effect. This presumably accounts for the observation of some high-field content in Hall-effect measurements in various metals up to $\sim 100°$K. In Cd, for example, Fig. 1 shows a small field-dependent contribution from high-field effects is detectable to $\rho_{21}(T)$ up to $\approx 140°$K.

[24] J. E. A. Alderson and C. M. Hurd, Can. J. Phys. 48, 2162 (1970); Phys. Rev. B 7, 1226 (1973).

[25] Equation (1) of Ref. 12, except for the detail that the subscripts i,j on the left-hand side of their version are printed in the wrong order.